First-principles design of high-temperature phonon-mediated superconductivity in two-dimensional Dirac semimetal $Mg_2B_4C_2$

Sobhit Singh[1], Aldo H. Romero[2], J. Mella[3,4], Vitalie Eremeev[5], Enrique Muñoz[6], Anastassia N. Alexandrova[7,8], Karin M. Rabe[1], David Vanderbilt[1], and F. Muñoz[3,4]
[1]*Department of Physics and Astronomy, Rutgers University, Piscataway, NJ, USA.*
[2]*Department of Physics, West Virginia University, West Virginia, USA.*
[3]*Departamento de Física, Facultad de Ciencias, Universidad de Chile, Santiago, Chile.*
[4]*Center for the Development of Nanoscience and Nanotechnology (CEDENNA), Santiago, Chile.*
[5]*Faculty of Engineering, Universidad Diego Portales, Santiago, Chile.*
[6]*Institute of Physics, Pontificia Universidad Católica de Chile, Santiago, Chile.*
[7]*Chemistry and Biochemistry, University of California, Los Angeles, USA. and*
[8]*California NanoSystems Institute, Los Angeles, California 90095, USA.*
(Dated: August 7, 2020)

A new two-dimensional material – $Mg_2B_4C_2$, belonging to the family of the conventional superconductor MgB_2, is theoretically predicted to exhibit superconductivity with record critical temperature T_c estimated in 67–84 K range (predicted using the isotropic Migdal-Eliashberg theory) without any tuning of external parameters such as doping, strain, or substrate-induced effects. The origin of such a high intrinsic T_c is ascribed to the presence of strong electron-phonon coupling and topological Dirac states (which are absent in MgB_2) yielding large density of states near the Fermi level. This material also features a nontrivial electronic band topology exhibiting Dirac points, practically gapless Dirac nodal lines, and topological nontrivial edge states. Consequently, it is a potential candidate for realization of topological superconductivity in 2D. This system is obtained after replacing the chemically active boron layers in MgB_2 by chemically inactive boron-carbon layers. Hence, the surfaces of this material are inert. Our calculations confirm the stability of 2D $Mg_2B_4C_2$. We also find that the essential features of this material remain invariant when its thickness is increased by increasing the number of inner MgB_2 layers.

The discovery of highly crystalline two-dimensional (2D) superconductors [1–5], such as $NbSe_2$ monolayer [6–9], has provided new possibilities for van der Waals (vdW) heterostructures nano-engineering of novel insulator-superconductor interfaces [10] and 2D Josephson junctions, without the need of an insulating layer [11]. One main challenging issue in the realization of 2D superconductivity is that most of the well-known conventional bulk superconductors either do not superconduct or poorly superconduct when their dimensions are reduced [6–8, 12–16]. Although numerous 2D phonon-mediated superconductors have recently been predicted from the first-principles calculations, the highest predicted intrinsic T_c stayed around 20 K [17–23] (19 K for B_2C monolayer [20], and 19–25 K for borophenes [21], to name a few). Though in some cases T_c has been enhanced by means of the chemical doping, intercalation, strain, and/or substrate proximity effects [22, 24–30], it is essential to discover intrinsic 2D superconductors that exhibit high-T_c without any doping or tuning of external parameters (here high-T_c does not refer to unconventional superconductivity as in cuprates or iron-based superconductors [31]).

Among all the Bardeen–Cooper–Schrieffer (BCS) type conventional superconductors, MgB_2 stands out with a record T_c of 39 K, the highest reported T_c at zero-pressure [32–34]. Such a high-T_c in MgB_2 stems from the strong electron-phonon (el-ph) coupling occurring primarily due to the in-plane stretching of B-B bonds (*i.e.*, E_{2g} phonon modes), which strongly couple with the self-doped charge carriers from magnesium to boron atoms [25, 33–36]. Remarkably, only two (E_{2g}) out of total nine phonon modes contribute to $\sim$ 97% superconductivity in MgB_2 [33–42]. Once the fundamental mechanism of such a high T_c in bulk MgB_2 was understood, which by the way was a subject of intense research for over a decade period [25, 33–47], researchers started proposing novel ways to augment T_c through rational material design approach [24, 35, 41, 42, 48, 49]. Pickett and co-workers proposed that one can, in principle, achieve a much higher T_c (than 39 K) by designing a MgB_2-like material which has a similar Fermi surface as that of in MgB_2, and in which more than two phonon modes couple to the electronic states near the Fermi level, thereby, resulting in a sizable total el-ph coupling [24, 41, 42]. This idea has been employed for the rational design of new bulk superconductors with a good success rate [50–59].

Despite the large success with the bulk conventional superconductors, two-dimensional intrinsic superconductors having a high-T_c remained elusive. Notably, various attempts have been made to realize superconductivity in the 2D analogues of bulk MgB_2 [13, 49, 60–63]. On the one hand, Xu and Beckman proposed a quasi-2D MgB_2 nanosheet with inert surfaces, which turns out to be a semiconductor with a bandgap of 0.51 eV resulting from the quantum confinement effects [13]. On the other hand, Bekaert et al. reported that a considerably high-T_c of 20 K can be realized in monolayer MgB_2 with-

out surface passivation, *i.e.*, if only such a material with a highly chemically reactive surface could be made [62, 63]. While an experimental validation of the predicted T_c in monolayer MgB_2 is still missing, the aforementioned theoretical works markedly enhance our understanding of superconductivity in 2D materials.

In this work, we present a novel MgB_2-like 2D material – $Mg_2B_4C_2$, having charge neutral inert surfaces, which is predicted to superconduct at a strikingly high T_c in the 67–84 K range (predicted using the isotropic Migdal-Eliashberg theory [64–66]), the highest T_c yet reported for an intrinsic 2D material without any doping, strain or substrate-induced effects. The main advantageous feature in 2D $Mg_2B_4C_2$ is the fact that, unlike in bulk MgB_2, more than two phonon modes strongly couple to the electronic states near the Fermi level, thus, resulting in a substantially larger el-ph coupling ($\lambda = 1.75$) in monolayer $Mg_2B_4C_2$ compared to bulk MgB_2 ($\lambda_{bulk} = 0.73$ [36], and 0.61 [34]). Moreover, our calculations reveal nontrivial topological electronic features in $Mg_2B_4C_2$ exhibiting Dirac cones and practically gapless Dirac nodal lines at the corner points of the hexagonal Brillouin zone (BZ), which enormously enhance the density of states (DOS) near the Fermi level, hence, positively contributing towards a higher T_c.

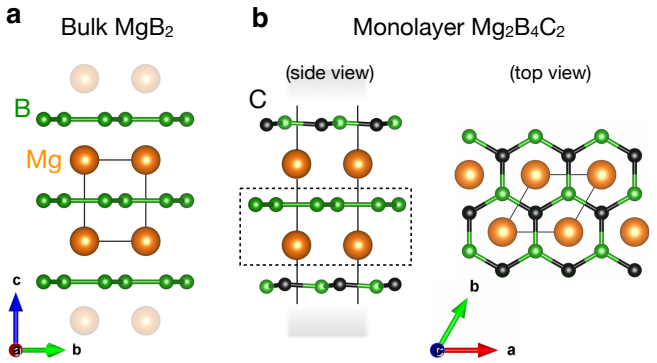

FIG. 1. Crystal structure. (**a**) bulk MgB_2, and (**b**) side (as viewed from $\vec{a}$) and top views of monolayer $Mg_2B_4C_2$ (Mg: orange, B: green, C: black). Solid black lines mark the unit cell boundaries, and shaded grey areas represent vacuum in the left panel of (**b**). The region marked by dashed black lines in (**b**) can be arbitrarily repeated (see text).

RESULTS

Material design strategy.

We start by describing our rationale for design of a stable MgB_2-like 2D superconductor having inert surfaces. Generally, layered vdW materials can be exfoliated to produce their 2D analogues [67]. Although bulk MgB_2 has a layered structure, it is not a vdW material. Bulk MgB_2 crystallizes in space group P_6/mmm (#191) containing alternating layers of Mg and B atoms stacked along the $\vec{c}$ lattice direction, as shown in Fig. 1(a) [40]. The bonding between the Mg and B atoms is purely ionic, which means that Mg atoms donate two electrons to B atoms, thereby making each Mg 2+ and each B 1−. Since a B^- is isoelectronic to a charge neutral carbon atom, a B-B sheet is structurally analogous to a single layer graphene, however, it has a different ordering of bands than that of in graphene. A simple exfoliation of MgB_2 into a 2D slab with B (or Mg) termination would yield a highly reactive electron-rich (or hole-rich) surface layer that is chemically unstable.

We propose that one can realize a charge-neutral slab of MgB_2 by substituting the top and bottom B-B surfaces with B-C layers. In other words, by replacing the exposed $(B\text{-}B)^-$ layer (note that the single negative charge arises from the missing Mg cations on the one side of the B-B sheet, but not on the other) with a charge-neutral B-C layer. Fig. 1(b) shows the top and side views of a $Mg_2B_4C_2$ monolayer designed using the aforementioned strategy. Strikingly, we find that repeating the intermediate Mg-B layers, *i.e.*, the layers sandwiched between the top and bottom surfaces (highlighted using dashed rectangle in Fig. 1(b)), thereby making thicker slabs of $(MgB_2)_nC_2$, n being the total number of Mg layers, retains the key features of the $Mg_2B_4C_2$ monolayer, as detailed in the Supplementary Material (SM) [68]. This feature could be particularly useful in the experimental realization of 2D superconductivity in $Mg_2B_4C_2$. Notably, the reported electronic properties are qualitatively valid for the rest of the $(MgB_2)_nC_2$ family (see SM [68] for details).

$Mg_2B_4C_2$ monolayer, shown in Fig. 1(b), belongs to the layer group $p\bar{3}m1$ (#72) having DFT (PBE) optimized lattice parameters $a = b = 2.87$ Å. The absolute thickness between the top and bottom atomic layers is 7.14 Å, whereas, the interlayer spacing between the adjacent Mg and B-B, and Mg and B-C (C-B) layers is ∼1.8 Å, and ∼1.7 Å, respectively. We note that the inversion symmetry is preserved due to the inverted ordering of the top and bottom layers in the structure shown in Fig. 1(b). However, one could break the inversion symmetry by replicating the top and bottom layers, *i.e.*, by making the top and bottom layers alike, either both as B-C or both as C-B. Our calculations suggest that the structure with inversion symmetry is energetically more favorable (5 meV/f.u.) than the structure with broken inversion symmetry; although both structures are dynamically, elastically, and mechanically stable since they exhibit all positive phonon frequencies, positive elastic constants, and satisfy the Born-Huang mechanical stability criteria (see SM [68]). The only qualitative difference in the electronic properties of the structure with broken inversion symmetry is a small lifting of some band degeneracies at the K high symmetry point (see SM [68]). This effect is analogous to the application of a perpendicular electrical field to a bilayer graphene [69]. In this article, hereafter, we focus only on a single layer of $Mg_2B_4C_2$ with preserved inversion symmetry.

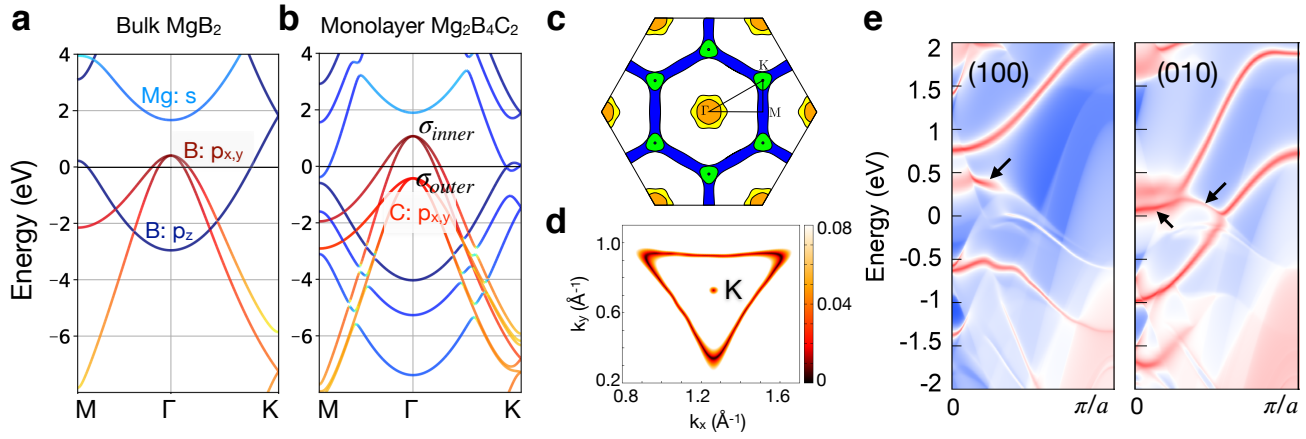

FIG. 2. Atomic orbitals projected electronic band structure of (**a**) bulk MgB_2, and (**b**) monolayer $Mg_2B_4C_2$ calculated without spin-orbit coupling (SOC) along the high symmetry direction of BZ. Cyan, red, and blue colors represent the contribution from the s, $p_{x,y}$, and p_z orbitals, respectively. See SM [68] for more details. (**c**) Calculated Fermi surface of monolayer $Mg_2B_4C_2$. Yellow/Orange, blue, and green colors depict hole, electron, and intertwined electron-hole pockets, respectively. (**d**) Energy bandgap (E_{gap}) plotted in color scale in the vicinity of a K high-symmetry point. Practically gapless Dirac nodal line centered at K (a small bandgap of ∼5 meV opens due to the subtle breaking of M_z mirror symmetry) and a gapless Dirac point at K can be noticed. (**e**) The local electronic density of states of the (100) and (010) edge states spectrum. Red/White color denotes the states near the edge/interior of the 2D system. Topological nontrivial edge states are marked using arrows.

Topological electronic properties of $Mg_2B_4C_2$ monolayer. After describing the crystal structure and its stability, we now focus on the topological electronic properties of $Mg_2B_4C_2$ monolayer. We begin by summarizing the key features of the electronic structure of bulk MgB_2 [40] from which $Mg_2B_4C_2$ monolayer is derived. As shown in Fig. 2(a), the Fermi surface of MgB_2 is composed of boron p orbitals, where $p_{x,y}$ orbitals hybridize with s orbitals to form strong covalent in-plane σ bonds at the zone center, while the unhybridized p_z orbitals form relatively weak out-of-plane π bonds at zone boundaries (Mg acts as electron donor). Due to such a distinct Fermi-surface geometry, two superconducting gaps exists in bulk MgB_2: (i) the stronger σ gap of ∼7 meV, and (ii) the weaker π gap of ∼2-3 meV [33, 34, 37, 44, 70–74]. Remarkably, different symmetries of the σ and π bonds largely suppress the impurity scattering in MgB_2 [37, 39, 40, 74].

Since the basic structure and charge neutrality of MgB_2 is preserved in monolayer $Mg_2B_4C_2$, the electronic band structure of monolayer $Mg_2B_4C_2$ qualitatively resembles with that of the bulk MgB_2, as shown in Fig. 2(a,b), but with some additional features. For instance, there is a new set of degenerate σ bands (σ_{outer}) present at Γ below the Fermi level arising from the $p_{x,y}$ orbitals of the outer boron-carbon layers. The other set of degenerate σ bands (σ_{inner}) at Γ that cross the Fermi level (also present in MgB_2) are formed by the $p_{x,y}$ orbitals of the inner boron-boron layer. These two sets of σ bands are almost parallel and split by ∼ 1.6 eV at Γ. Since the σ_{outer} bands are completely occupied, they should, in principle, have no contribution in superconductivity, unless there is a large external field applied in a FET-like geometry [75].

In addition to a new set of σ bands at Γ, we notice the presence of Dirac-like band crossings at the BZ corner, K point, as well as along the high-symmetry directions near the K point of monolayer $Mg_2B_4C_2$. We note that the Dirac crossing at K is also present in bulk MgB_2, but it is situated well-above the Fermi level. The Dirac-like band crossings in $Mg_2B_4C_2$ monolayer are formed by highly dispersing p_z orbitals of carbon and boron atoms (see SM [68] for details). Thus, the Fermi surface of $Mg_2B_4C_2$ monolayer, shown in Fig. 2(c), embodies three main features: (i) two hole pockets at Γ (one circular and another that takes the shape of the BZ) composed of σ bonded boron $p_{x,y}$ orbitals, (ii) an electron pocket at M formed by boron p_z orbitals, and (iii) intertwined electron and hole pockets at the K point and along K–M high-symmetry line, formed by π bonded carbon and boron p_z orbitals. We note that these pockets show very strong coupling to the phonon modes, and, as a result, they play the key role in governing superconductivity in $Mg_2B_4C_2$ monolayer, as we discuss later. Moreover, the sharp and well-defined (almost flat) boundaries of the charge-carrier pockets at the Fermi surface set up the stage for the possible realization of Kohn-like divergencies [76], and charge-density wave ordering [77, 78] in this 2D system, which is beyond the scope of present work and calls for a more comprehensive attention in future.

By plotting the energy bandgap (E_{gap}) distribution in the vicinity of the K points, we discover presence of a triangular nodal line in the vicinity of each K point, as shown in Fig. 2(d). However, this is not a truly gapless

nodal line since a small E_{gap} (∼5 meV) exists due to the subtle breaking of M_z mirror symmetry. It is worth noting that the Dirac point at K is topologically protected by the C_{3v} rotation, inversion, and time-reversal symmetries; a small gap opens at Dirac points when the inversion symmetry is broken by making the top and bottom B-C layers identical [68, 79]. Although there are theoretical proposals suggesting the possibility of topological superconductivity in Dirac semimetals [80], we think that the so-far studied models are quite simple, and this topic requires a more comprehensive examination before any exotic effects can be confidently claimed here.

In order to prove the nontrivial topological nature of Dirac points, we compute the Berry phase along a k-line enclosing the gapless point at K. Our calculations yield a nontrivial Berry phase of π. The inversion-symmetry of $Mg_2B_4C_2$ monolayer further enables us to determine the Z_2 topological invariants using the Fu-Kane criterion [81]. The inversion parity eigenvalues of the electronic wavefunction of all 12 occupied bands at four time-reversal invariant momenta (TRIM) points are given in Table I. The product of all parity eigenvalues (δ) at each TRIM is also listed in Table I. We find that the Z_2 topological index is nontrivial due to δ = -1 at three TRIM points. Here, we note that bulk MgB_2 has a weak Z_2 topological index (0; 001) due to the band-inversions occurring at the Γ and A (0, 0, 0.5) high-symmetry points of 3D hexagonal BZ [82]. Robust topological surface states have recently been experimentally observed in MgB_2 [83].

TABLE I. Parity eigenvalues of all occupied bands and their products at four TRIM points

TRIM	Parity eigenvalues	δ
Γ (0, 0, 0)	+ − + − + − + + − − ++	−1
M_1 (0.5, 0.0, 0.0)	− + − + − + + − + − −−	−1
M_2 (0.0, 0.5, 0.0)	− + − + − + + − + − −−	−1
M_3 (0.5, 0.5, 0.0)	− + − + − + + − + − −+	+1

Since the nontrivial topology in 2D systems is often manifested in the gapless 1D edge states, we further confirm the nontrivial topological features of monolayer $Mg_2B_4C_2$ by computing the local density of states at (100) and (010) edges of 60 unit cell thick nano-ribbons. Topologically nontrivial 1 D edge states connecting band-crossing points were obtained at both (100) and (010) edges, as shown in Fig. 2(e), thus, proving the nontrivial topology of the $Mg_2B_4C_2$ monolayer.

Electron-phonon coupling and superconductivity in $Mg_2B_4C_2$. We find that the roots of superconductivity in $Mg_2B_4C_2$ monolayer are same as in bulk MgB_2 [33–42]. However, the main advantageous factor in $Mg_2B_4C_2$ is that, in addition to the doubly degenerate E_{2g} modes that govern superconductivity in MgB_2, numerous other phonon modes strongly couple to the electronic states near the Fermi level yielding a much larger overall el-ph coupling, and thus, resulting in a considerably higher T_c..

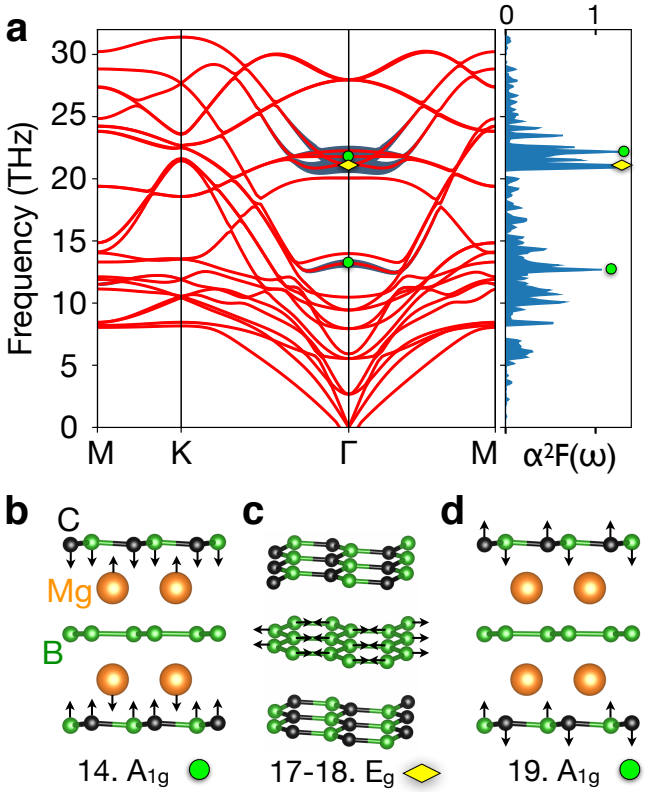

FIG. 3. (**a**) Calculated phonon spectrum of $Mg_2B_4C_2$ monolayer with phonon linewidths $\lambda(\mathbf{q}, n)$ projected using shaded colors. To avoid large overlap of $\lambda(\mathbf{q}, n)$ with the phonon spectra, we have divided the intensity by a factor of four. Green circles and yellow diamond mark the three phonon modes at Γ, two nondegenerate A_{1g} (out-of-plane) and one doubly degenerate E_g (in-plane) modes, that exhibit the largest el-ph coupling. Several other phonon modes, not marked here, also exhibit decent amount of el-ph coupling with a relatively smaller magnitude (see SM [68]), as evident in the Migdal-Eliashberg spectral function (a.u.) plot on the right panel of (**a**). (**b**, **c**, **d**) Visualization of the atomic vibrations corresponding to the aforementioned three phonon modes at Γ. The numerals 14, 17-18, and 19 denote the phonon mode index as counted from the lowest to the highest frequency modes (*i.e.*, 1-3 for acoustic modes). Mg atoms are omitted in (**c**) for the sake of clarity.

The calculated phonon spectrum of $Mg_2B_4C_2$ monolayer, shown in Fig. 3(a), contains a total of 24 phonon modes (8 atoms/cell) having the following mode symmetry at Γ:

$$\begin{aligned} \Gamma_{\text{acoustic}} &= A_{2u} + E_u, \\ \Gamma_{\text{optic}} &= 4A_{1g} + 3A_{2u} + 3E_u + 4E_g. \end{aligned} \tag{1}$$

Here, A_{1g} and E_g are Raman-active modes, whereas, A_{2u} and E_u are infrared-active modes. In Fig. 3(b-d), we

show the atomic vibration patterns for the three phonon modes, namely, two nondegenerate A_{1g} modes (index 14 and 19) and one degenerate E_g mode (indices 17-18), which exhibit the largest el-ph coupling (details regarding all other phonon modes are provided in the SM [68]). Both A_{1g} modes correspond to the out-of-plane vibration of the Mg and outer B-C layers, while the E_g mode corresponds to the in-plane stretching of the inner B-B layer. The A_{1g} modes (indices 14, 19) modulate the el-ph coupling associated with the π bonded p_z orbitals contributing to the electron and hole pockets located at the BZ boundaries. Whereas, the doubly degenerate E_g mode (indices 17-18) couples with the σ bonded $p_{x,y}$ orbitals forming the hole pockets located at Γ. Here, it is worth noting that the higher frequency E_g modes (indices 21-22) that corresponds to the in-plane stretching of the outer B-C layers do not make a significant contribution to the overall el-ph in this system, which is as expected since these modes modulate the σ_{outer} bands located well-below the Fermi level at Γ (see Fig. 2(b)).

Since the electronic and vibrational band structures of inner B-B and outer B-C layers are essentially independent of each other, we predicate that the reported properties of the studied $Mg_2B_4C_2$ monolayer would be retained even when the number of the inner B-B layers are repeated (until a critical thickness), thus making the system thicker. This feature might greatly simplify the eventual realization of superconductivity in $Mg_2B_4C_2$.

To quantify the superconducting properties of $Mg_2B_4C_2$ monolayer, we follow the Migdal-Eliashberg formalism [64–66], which relies on the calculation of the el-ph coupling matrix elements within DFT. The calculated matrix elements correspond to the transition probabilities of different Kohn-Sham states induced by a change in the potential due to a small ionic displacement. Thus, these matrix elements provide the main ingredients to calculate the el-ph coupling strength and the Eliashberg spectral function $\alpha^2F(\omega)$ as a function of the phonon frequency ω. Since the physical process behind the phonon-mediated superconductivity is the exchange of a phonon between two electrons, a strong el-ph coupling is desired to achieve a large-T_c in a BCS superconductor. Theoretical details of such calculations are explained in numerous other papers [71, 84, 85].

In Fig. 3(a), we project the calculated phonon linewidth $\lambda(\mathbf{q}, n)$ for each phonon mode n at each wave vector $\mathbf{q}$. Note that the projected phonon linewidth is scaled down by a factor of four to avoid large overlap with the neighboring phonon branches. The largest contribution to the el-ph coupling strength comes from the three modes, namely, two nondegenerate A_{1g} modes (index 14 and 19), and one doubly degenerate E_g mode (indices 17-18), as marked in Fig. 3(a) and discussed above. The large el-ph coupling is also manifested in the anomalous softening of these phonon modes near Γ. In addition to these phonon modes, various other modes also make relatively smaller contributions to the overall el-ph coupling strength, as revealed by the Eliashberg spectral function $\alpha^2F(\omega)$ plot shown in the side panel of Fig. 3(a).

In order to investigate the role of anharmonic effects on the el-ph coupling, we have thoroughly studied phonon-phonon (ph-ph) interactions by computing ph-ph linewidths using the *ab-initio* molecular dynamics simulations. In this approach, we mapped the forces, obtained from the finite-temperature molecular dynamics simulations, evaluated in a $3 \times 3 \times 1$ supercell onto a model Hamiltonian describing the lattice dynamics. This temperature dependent effective potential (TDEP) technique [86, 87] enabled us to calculate the third-order response from the effective renormalized interatomic force constants. Our calculations revealed that the ph-ph linewidths are an order of magnitude smaller than the el-ph linewidths. The maximum value of obtained ph-ph linewidths is $\sim$2 meV, which is much smaller compared to the el-ph linewidth values that are typically larger than $\sim$70 meV in the studied system. This result implies that, although the system inherits some anharmonic effects, we can safely discard the ph-ph contributions in the study of its superconducting properties.

Based on the BCS theory of superconductivity and above results, we estimate the critical temperature T_c using the McMillian-Allen-Dynes formula [88–90]:

$$T_c = \frac{\omega_{log}}{1.2} exp\left[-\frac{1.04(1+\lambda)}{\lambda - \mu^*(1+0.62\lambda)}\right], \tag{2}$$

where ω_{log} is the logarithmic averaged phonon frequency, λ is the total el-ph coupling constant, and μ^* is the effective screened Coulomb repulsion constant which is a tunable parameter with a typical value ranging from 0.05–0.20 (see Table II) [20, 33, 34, 36, 53]. We obtain λ by integrating the cumulative frequency-dependent el-ph coupling $\lambda(\omega)$ given by the following expression:

$$\lambda(\omega) = 2\int_0^{\omega} \frac{\alpha^2F(\omega)}{\omega} d\omega \tag{3}$$

We find a fairly large value of $\lambda = 1.75$, which is considerably larger than that of reported for bulk MgB_2 ($\lambda_{bulk} = 0.73$ [36], and 0.61 [34]). The estimation of T_c requires the knowledge of μ^*, which is an adjustable parameter. For isotropic $\mu^* = 0.05$, 0.10, 0.135, and 0.20 values, our calculations predict $T_c = 83.5$, 74.3, 67.0, and 55.6 K, respectively. We note that for bulk MgB_2, $\mu^* = 0.05$ has been used to get the correct estimate of $T_c = 40$ K [36]. Therefore, using the isotropic Migdal-Eliashberg theory, we estimate the T_c of $Mg_2B_4C_2$ monolayer to be in range 67–84 K. In passing, we would like to mention that the predicted T_c could moderately vary if an anisotropic Migdal-Eliashberg theory is employed [34].

In order to highlight the novelty of our results, we have listed the theoretical superconducting parameters along with the estimated T_c for some reported 2D phonon-

TABLE II. Listing of superconducting parameters required for the prediction of T_c within isotropic Migdal-Eliashberg theory for some reported 2D phonon-mediated superconductors. This table includes data of effective Coulomb screening parameter μ^*, electronic DOS at the Fermi level $N(\mathrm{E}_F)$ (in states/spin/Ry/cell), logarithmic averaged phonon frequency ω_{log} (in K), total electron-phonon coupling constant λ, and estimated T_c (in K). Experimental T_c values are noted in the table.

Compounds	μ^*	$N(\mathrm{E}_F)$	ω_{log}	λ	T_c	Ref.
B_2C	0.10		315	0.92	19	[20]
CaC_6	0.115		446	0.40	1.4	[91]
LiC_6	0.115		400	0.61	8.1	[91]
LiC_6				0.58 ± 0.05	5.9 [Exp.]	[92]
LiC_6	0.12/0.14/0.16			0.55	7.6/5.9/5.1	[93]
2H-$NbSe_2$				0.75	3.1 [Exp.]	[7]
2H-$NbSe_2$	0.15, 0.16		134, 145	0.84, 0.67	4.5, 2.7	[94, 95]
C_6CaC_6					4.0 [Exp.]	[96]
C_6CaC_6	0.207/0.155				6.8/8.1	[97]
B(β_{12})	0.10–0.15	8.12	425	0.69	14	[98]
B(α)	0.05	5.85	262	0.52	7	[99]
Borophene	0.10		421	0.79	19	[100]
Borophene	0.10			0.6-1.1	10–20	[17]
Li_2B_7	0.12		463	0.56	6	[101]
$TiSi_4$	0.10			0.59	5.8	[29]
Mo_2C	0.10			0.63	5.9	[30]
Cu-BHT	0.10		51.8	1.16	4.43	[102]
β_0-PC	0.10	7.27	118	1.48	13.4	[18]
tetr-Mo_2B_2	0.10	16.02	345	0.49	4	[103]
tri-Mo_2B_2	0.10	16.81	295	0.30	0.2	[103]
tetr-W_2B_2	0.10	12.46	232	0.69	8	[23]
hex-W_2B_2	0.10	13.60	232	0.43	1.5	[23]
strained-YS	0.10	0.75–1.05	243–100	0.20–0.90	0–6	[23]
	0.05				84	Our work
$Mg_2B_4C_2$	0.10	13.7	570	1.75	74	Our work
	0.135				67	Our work

mediated superconductors in Table II. The good agreement between the experimental data for LiC_6 [91–93], 2H-$NbSe_2$ [7, 94, 95], and C_6CaC_6 [96, 97] and the associated theoretical results obtained from the Migdal-Eliashberg theory further boosts our confidence in our predictions.

In summary, we present a 2D material $Mg_2B_4C_2$, similar to MgB_2, but with inert surfaces obtained by the replacement of outer B-B layers by B-C layers. Our calculations suggest that this structure is dynamically, elastically and mechanically stable. It also features a nontrivial topological electronic band structure together with a large el-ph coupling ($\lambda = 1.75$), which is more than twice as large as that of bulk MgB_2. Use of the standard isotropic Migdal-Eliashberg theory predicts the superconducting transition temperature T_c to be in the range of 67–84 K without any doping or tuning of external parameters such as strain. To the best of our knowledge, this is the highest predicted intrinsic T_c in a conventional BCS-type 2D superconductor to date. The studied material offers the two expected ingredients: (i) topological nontrivial electronic properties, and (ii) large intrinsic T_c, for practical realization of nontrivial topological superconductivity in 2D [104]. In addition to the large el-ph coupling, the presence of sharp and well-defined flat boundaries of the charge-carrier pockets at the Fermi surface imply the possible realization of Kohn-like divergencies and charge-density wave ordering in this 2D system, which calls for a dedicated study in future.

Acknowledgments. This work was supported in part by Fondecyt Grants No. 1191353 and Center for the Development of Nanoscience and Nanotechnology CEDENNA FB0807. S.S. and D.V acknowledge the support from ONR Grant N00014-16-1-2951. We also thank the NSF CAREER Award CHE-1351968 to A.N.A and DMREF-NSF 1434897, NSF OAC-1740111 and DOE DE-SC0016176 projects to A.H.R. This research was partially supported by the supercomputing infrastructure of the NLHPC (ECM-02) and XSEDE which is supported by National Science Foundation grant number ACI-1053575. The authors also acknowledge the support from the Texas Advances Computer Center (with the Stampede2 and Bridges supercomputers).

METHODS

The electronic bands structure and phonon calculations were performed using density-functional theory (DFT) as implemented in the VASP package [105–108]. The phonopy [109] and PyProcar [110] tools were used for the post-processing of data. The PBE exchange-correlation functional [111] and PAW pseudopotentials [112, 113] were used. The employed k-point grid for self-consistent calculations was 30×30, and the cutoff for the kinetic energy of plane waves was set to 700 eV. A vacuum of thickness 30 Å was added to avoid the periodic interactions along the c-axis. Since the spin-orbit coupling (SOC) effects were found to be negligible in the studied system, SOC was not included in the reported calculations. The elastic and mechanical properties were analyzed using the MechElastic code [114]. The topological properties of $Mg_2B_4C_2$ were studied by fitting the DFT calculated bandstructure to a real space tight-binding Hamiltonian obtained using the maximally localized Wannier functions (MLWFs) approach [115, 116]. The local density of states at (100) and (010) edges were calculated for 60 unit cells thick nano-ribbons using the WannierTools package [116] with vacuum added along the c-axis of the ribbon.

For the electron-phonon coupling matrix elements calculations, we used the current implementation in the abinit package [117–121]. We used norm conserving pseudopotentials (using the ONCVPSP scheme of Hamann [122]), and a plane wave basis set up to kinetic energies of 35 Ha. Cell parameters were optimized by using the PBE exchange-correlation functional as in VASP calculations. We used a uniform grid of $16\times16\times1$ for the ground state calculations, and a phonon grid of $4\times4\times1$ for the phonon part. A total of 240 el-ph matrix elements were calculated. Calculations of the phonon interatomic force constants, and the el-ph coupling matrix elements performed in this work used the second-order perturbation theory [123, 124]. The temperature dependent effective potential (TDEP) technique [86, 87] was used to study the phonon-phonon interactions and phonon anharmonic effects.

[1] T. Uchihashi, Supercond. Sci. Technol. **30**, 013002 (2017).
[2] Y. Saito, T. Nojima, and Y. Iwasa, Nat. Rev. Mater. **2**, 16094 (2017).
[3] D. Jiang, T. Hu, L. You, Q. Li, A. Li, H. Wang, G. Mu, Z. Chen, H. Zhang, G. Yu, J. Zhu, Q. Sun, C. Lin, H. Xiao, X. Xiaoming, and J. Mianheng, Nat Commun. **5**, 5708 (2014).
[4] Y. Kamihara, T. Watanabe, M. Hirano, and H. Hosono, Journal of the American Chemical Society **130**, 3296 (2008).
[5] C. Brun, T. Cren, and D. Roditchev, Superconductor Science and Technology **30**, 013003 (2016).
[6] R. F. Frindt, Phys. Rev. Lett. **28**, 299 (1972).
[7] X. Xi, L. Zhao, Z. Wang, H. Berger, L. Forró, J. Shan, and K. F. Mak, Nat. Nanotechnol. **10**, 765 (2015).
[8] M. M. Ugeda, A. J. Bradley, Y. Zhang, S. Onishi, Y. Chen, W. Ruan, C. Ojeda-Aristizabal, H. Ryu, M. T. Edmonds, H.-Z. Tsai, *et al.*, Nat. Phys. **12**, 92 (2016).
[9] Y.-L. Li, E. Stavrou, Q. Zhu, S. M. Clarke, Y. Li, and H.-M. Huang, Phys. Rev. B **99**, 220503 (2019).
[10] K. S. Novoselov, A. Mishchenko, A. Carvalho, and A. H. Castro Neto, Science **353** (2016).
[11] N. Yabuki, R. Moriya, M. Arai, Y. Sata, S. Morikawa, S. Masubuchi, and T. Machida, Nat. Commun. **7**, 10616 (2016).
[12] X. Xi, Z. Wang, W. Zhao, J.-H. Park, K. T. Law, H. Berger, L. Forró, J. Shan, and K. F. Mak, Nature Physics **12**, 139 (2016).
[13] B. Z. Xu and S. P. Beckman, 2D Mater. **3**, 031003 (2016).
[14] S. C. de la Barrera, M. R. Sinko, D. P. Gopalan, N. Sivadas, K. L. Seyler, K. Watanabe, T. Taniguchi, A. W. Tsen, X. Xu, D. Xiao, and B. M. Hunt, Nature Communications **9**, 1427 (2018).
[15] L. Bao, Y. Bi, X. Liu, X. Yang, T. Hao, S. Tian, Z. Wang, J. Li, and C. Gu, Applied Physics Letters **113**, 022603 (2018).
[16] R. Yan, G. Khalsa, B. T. Schaefer, A. Jarjour, S. Rouvimov, K. C. Nowack, H. G. Xing, and D. Jena, Applied Physics Express **12**, 023008 (2019).
[17] E. S. Penev, A. Kutana, and B. I. Yakobson, Nano Lett. **16**, 2522 (2016).
[18] B.-T. Wang, P.-F. Liu, T. Bo, W. Yin, O. Eriksson, J. Zhao, and F. Wang, Phys. Chem. Chem. Phys. **20**, 12362 (2018).
[19] J. Lei, A. Kutana, and B. I. Yakobson, J. Mater. Chem. C **5**, 3438 (2017).
[20] J. Dai, Z. Li, J. Yang, and J. Hou, Nanoscale **4**, 3032 (2012).
[21] M. Gao, Q.-Z. Li, X.-W. Yan, and J. Wang, Phys. Rev. B **95**, 024505 (2017).
[22] Z. Qu, S. Lin, M. Xu, J. Hao, J. Shi, W. Cui, and Y. Li, J. Mater. Chem. C **7**, 11184 (2019).
[23] L. Yan, T. Bo, W. Zhang, P.-F. Liu, Z. Lu, Y.-G. Xiao, M.-H. Tang, and B.-T. Wang, Phys. Chem. Chem. Phys. **21**, 15327 (2019).
[24] H. Rosner, A. Kitaigorodsky, and W. E. Pickett, Phys. Rev. Lett. **88**, 127001 (2002).
[25] A. V. Pogrebnyakov, J. M. Redwing, S. Raghavan, V. Vaithyanathan, D. G. Schlom, S. Y. Xu, Q. Li, D. A. Tenne, A. Soukiassian, X. X. Xi, M. D. Johannes, D. Kasinathan, W. E. Pickett, J. S. Wu, and J. C. H. Spence, Phys. Rev. Lett. **93**, 147006 (2004).
[26] T. E. Weller, M. Ellerby, S. S. Saxena, R. P. Smith, and N. T. Skipper, Nature Physics **1**, 39 (2005).
[27] A. Gauzzi, S. Takashima, N. Takeshita, C. Terakura, H. Takagi, N. Emery, C. Hérold, P. Lagrange, and G. Loupias, Phys. Rev. Lett. **98**, 067002 (2007).
[28] G. Savini, A. C. Ferrari, and F. Giustino, Phys. Rev. Lett. **105**, 037002 (2010).
[29] Q. Wu, J.-J. Zhang, P. Hao, Z. Ji, S. Dong, C. Ling, Q. Chen, and J. Wang, *The Journal of Physical Chemistry Letters*, The Journal of Physical Chemistry Letters **7**, 3723 (2016).

[30] J.-J. Zhang and S. Dong, The Journal of Chemical Physics **146**, 034705 (2017).
[31] S. P. Kruchinin, Reviews in Theoretical Science **2**, 124 (2014).
[32] J. Nagamatsu, N. Nakagawa, T. Muranaka, Y. Zenitani, and J. Akimitsu, Nature **410**, 63 (2001).
[33] H. J. Choi, D. Roundy, H. Sun, M. L. Cohen, and S. G. Louie, Nature **418**, 758 (2002).
[34] H. J. Choi, D. Roundy, H. Sun, M. L. Cohen, and S. G. Louie, Phys. Rev. B **66**, 020513 (2002).
[35] J. M. An and W. E. Pickett, Phys. Rev. Lett. **86**, 4366 (2001).
[36] K.-P. Bohnen, R. Heid, and B. Renker, Phys. Rev. Lett. **86**, 5771 (2001).
[37] M. Iavarone, G. Karapetrov, A. E. Koshelev, W. K. Kwok, G. W. Crabtree, D. G. Hinks, W. N. Kang, E.-M. Choi, H. J. Kim, H.-J. Kim, and S. I. Lee, Phys. Rev. Lett. **89**, 187002 (2002).
[38] W. Pickett, Nature **418**, 733 (2002).
[39] I. Mazin and V. Antropov, Physica C Supercond. **385**, 49 (2003).
[40] X. X. Xi, Rep. Prog. Phys. **71**, 116501 (2008).
[41] W. Pickett, Physica C: Superconductivity **468**, 126 (2008).
[42] W. E. Pickett, Journal of Superconductivity and Novel Magnetism **19**, 291 (2006).
[43] T. Yildirim, O. Gülseren, J. W. Lynn, C. M. Brown, T. J. Udovic, Q. Huang, N. Rogado, K. A. Regan, M. A. Hayward, J. S. Slusky, T. He, M. K. Haas, P. Khalifah, K. Inumaru, and R. J. Cava, Phys. Rev. Lett. **87**, 037001 (2001).
[44] P. Szabó, P. Samuely, J. Kačmarčík, T. Klein, J. Marcus, D. Fruchart, S. Miraglia, C. Marcenat, and A. G. M. Jansen, Phys. Rev. Lett. **87**, 137005 (2001).
[45] H. Rosner, J. M. An, W. E. Pickett, and S.-L. Drechsler, Phys. Rev. B **66**, 024521 (2002).
[46] H. J. Choi, M. L. Cohen, and S. G. Louie, Physica C Supercond. **385**, 66 (2003).
[47] J. Kortus, Physica C Supercond. **456**, 54 (2007).
[48] W. Pickett, B. Klein, and D. Papaconstantopoulos, Physica B+C **107**, 667 (1981).
[49] W. Pickett, J. An, H. Rosner, and S. Savrasov, Physica C: Superconductivity **387**, 117 (2003).
[50] A. K. Verma, P. Modak, D. M. Gaitonde, R. S. Rao, B. K. G. odwal, and L. C. Gupta, EPL **63**, 743 (2003).
[51] H. Rosner, A. Kitaigorodsky, and W. Pickett, Phys. Rev. Lett. **88**, 1270011 (2002).
[52] J. M. An, S. Y. Savrasov, H. Rosner, and W. E. Pickett, Phys. Rev. B **66**, 220502 (2002).
[53] H. J. Choi, S. G. Louie, and M. L. Cohen, Phys. Rev. B **80**, 064503 (2009).
[54] R. Miao, G. Huang, and J. Yang, Solid State Commun. **233**, 30 (2016).
[55] C. Bersier, A. Floris, A. Sanna, G. Profeta, A. Continenza, E. K. U. Gross, and S. Massidda, Phys. Rev. B **79**, 104503 (2009).
[56] M. R. Norman, Rep. Prog. Phys. **79**, 074502 (2016).
[57] V. Stanev, C. Oses, A. G. Kusne, E. Rodriguez, J. Paglione, S. Curtarolo, and I. Takeuchi, npj Computational Materials **4**, 29 (2018).
[58] H. Zhai, F. Munoz, and A. N. Alexandrova, J. Mater. Chem. C **7**, 10700 (2019).
[59] M. Klintenberg and O. Eriksson, Comput. Mater. Sci. **67**, 282 (2013).
[60] M. Naito and K. Ueda, Superconductor Science and Technology **17**, R1 (2004).
[61] X. X. Xi, Superconductor Science and Technology **22**, 043001 (2009).
[62] J. Bekaert, A. Aperis, B. Partoens, P. M. Oppeneer, and M. V. Milošević, Phys. Rev. B **96**, 094510 (2017).
[63] J. Bekaert, L. Bignardi, A. Aperis, P. van Abswoude, C. Mattevi, S. Gorovikov, L. Petaccia, A. Goldoni, B. Partoens, P. Oppeneer, *et al.*, Sci. Rep. **7**, 14458 (2017).
[64] A. Migdal, Sov. Phys. JETP **7**, 996 (1958).
[65] G. Eliashberg, Sov. Phys. JETP **11**, 696 (1960).
[66] P. B. Allen and B. Mitrović (Academic Press, 1983) pp. 1 – 92.
[67] A. K. Geim and I. V. Grigorieva, Nature **499**, 419 (2013).
[68] "See Supplemental Material (SM) at href for our results on the structure with broken inversion symmetry, thicker slabs, and more details on the electronic band structure, tight-binding model, and phonons.".
[69] J. Li, I. Martin, M. Büttiker, and A. F. Morpurgo, Phys. Scr. **2012**, 014021 (2012).
[70] M. Iavarone, G. Karapetrov, A. Koshelev, W. K. Kwok, D. Hinks, G. W. Crabtree, W. N. Kang, E.-M. Choi, H. J. Kim, and S.-I. Lee, Superconductor Science and Technology **16**, 156 (2002).
[71] E. R. Margine and F. Giustino, Phys. Rev. B **87**, 024505 (2013).
[72] D. Mou, R. Jiang, V. Taufour, S. L. Bud'ko, P. C. Canfield, and A. Kaminski, Phys. Rev. B **91**, 214519 (2015).
[73] A. Aperis, P. Maldonado, and P. M. Oppeneer, Phys. Rev. B **92**, 054516 (2015).
[74] J. Kortus, I. I. Mazin, K. D. Belashchenko, V. P. Antropov, and L. L. Boyer, Phys. Rev. Lett. **86**, 4656 (2001).
[75] J. T. Ye, Y. J. Zhang, R. Akashi, M. S. Bahramy, R. Arita, and Y. Iwasa, Science **338**, 1193 (2012).
[76] W. Kohn, Phys. Rev. Lett. **2**, 393 (1959).
[77] G. Grüner, Rev. Mod. Phys. **60**, 1129 (1988).
[78] X. Zhu, Y. Cao, J. Zhang, E. W. Plummer, and J. Guo, Proceedings of the National Academy of Sciences **112**, 2367 (2015).
[79] Q. D. Gibson, L. M. Schoop, L. Muechler, L. S. Xie, M. Hirschberger, N. P. Ong, R. Car, and R. J. Cava, Phys. Rev. B **91**, 205128 (2015).
[80] S. Kobayashi and M. Sato, Phys. Rev. Lett. **115**, 187001 (2015).
[81] L. Fu and C. L. Kane, Phys. Rev. B **76**, 045302 (2007).
[82] K.-H. Jin, H. Huang, J.-W. Mei, Z. Liu, L.-K. Lim, and F. Liu, npj Computational Materials **5**, 57 (2019).
[83] X. Zhou, K. N. Gordon, K.-H. Jin, H. Li, D. Narayan, H. Zhao, H. Zheng, H. Huang, G. Cao, N. D. Zhigadlo, F. Liu, and D. S. Dessau, Phys. Rev. B **100**, 184511 (2019).
[84] F. Giustino, Rev. Mod. Phys. **89**, 015003 (2017).
[85] F. Giustino, M. L. Cohen, and S. G. Louie, Phys. Rev. B **76**, 165108 (2007).
[86] O. Hellman and I. A. Abrikosov, Phys. Rev. B **88**, 144301 (2013).
[87] O. Hellman, P. Steneteg, I. A. Abrikosov, and S. I. Simak, Phys. Rev. B **87**, 104111 (2013).
[88] J. Bardeen, L. N. Cooper, and J. R. Schrieffer, Phys. Rev. **108**, 1175 (1957).
[89] W. L. McMillan, Phys. Rev. **167**, 331 (1968).

[90] P. B. Allen and R. C. Dynes, Phys. Rev. B **12**, 905 (1975).
[91] G. Profeta, M. Calandra, and F. Mauri, Nature Physics **8**, 131 (2012).
[92] B. M. Ludbrook, G. Levy, P. Nigge, M. Zonno, M. Schneider, D. J. Dvorak, C. N. Veenstra, S. Zhdanovich, D. Wong, P. Dosanjh, C. Straßer, A. Stöhr, S. Forti, C. R. Ast, U. Starke, and A. Damascelli, Proceedings of the National Academy of Sciences **112**, 11795 (2015).
[93] J.-J. Zheng and E. R. Margine, Phys. Rev. B **94**, 064509 (2016).
[94] C.-S. Lian, C. Si, and W. Duan, *Nano Letters*, Nano Letters **18**, 2924 (2018).
[95] F. Zheng and J. Feng, Phys. Rev. B **99**, 161119 (2019).
[96] S. Ichinokura, K. Sugawara, A. Takayama, T. Takahashi, and S. Hasegawa, *ACS Nano*, ACS Nano **10**, 2761 (2016).
[97] E. R. Margine, H. Lambert, and F. Giustino, Scientific Reports **6**, 21414 (2016).
[98] C. Cheng, J.-T. Sun, H. Liu, H.-X. Fu, J. Zhang, X.-R. Chen, and S. Meng, 2D Materials **4**, 025032 (2017).
[99] Y. Zhao, S. Zeng, and J. Ni, Phys. Rev. B **93**, 014502 (2016).
[100] R. C. Xiao, D. F. Shao, W. J. Lu, H. Y. Lv, J. Y. Li, and Y. P. Sun, Applied Physics Letters **109**, 122604 (2016).
[101] C. Wu, H. Wang, J. Zhang, G. Gou, B. Pan, and J. Li, *ACS Applied Materials & Interfaces*, ACS Applied Materials & Interfaces **8**, 2526 (2016).
[102] X. Zhang, Y. Zhou, B. Cui, M. Zhao, and F. Liu, *Nano Letters*, Nano Letters **17**, 6166 (2017).
[103] L. Yan, T. Bo, P.-F. Liu, B.-T. Wang, Y.-G. Xiao, and M.-H. Tang, J. Mater. Chem. C **7**, 2589 (2019).
[104] X.-L. Qi and S.-C. Zhang, Rev. Mod. Phys. **83**, 1057 (2011).
[105] G. Kresse and J. Hafner, Phys. Rev. B **47**, 558 (1993).
[106] G. Kresse and J. Hafner, Phys. Rev. B **49**, 14251 (1994).
[107] G. Kresse and J. Furthmüller, Comput. Mat. Sci. **6**, 15 (1996).
[108] G. Kresse and J. Furthmüller, Phys. Rev. B **54**, 11169 (1996).
[109] A. Togo and I. Tanaka, Scr. Mater. **108**, 1 (2015).
[110] U. Herath, P. Tavadze, X. He, E. Bousquet, S. Singh, F. Muñoz, and A. H. Romero, Computer Physics Communications **251**, 107080 (2020).
[111] J. P. Perdew, K. Burke, and M. Ernzerhof, Phys. Rev. Lett. **77**, 3865 (1996).
[112] P. E. Blöchl, Phys. Rev. B **50**, 17953 (1994).
[113] G. Kresse and D. Joubert, Phys. Rev. B **59**, 1758 (1999).
[114] S. Singh, I. Valencia-Jaime, O. Pavlic, and A. H. Romero, Phys. Rev. B **97**, 054108 (2018).
[115] A. A. Mostofi, J. R. Yates, G. Pizzi, Y.-S. Lee, I. Souza, D. Vanderbilt, and N. Marzari, Comput. Phys. Commun. **185**, 2309 (2014).
[116] Q. Wu, S. Zhang, H.-F. Song, M. Troyer, and A. A. Soluyanov, Comput. Phys. Commun. **224**, 405 (2018).
[117] X. Gonze, J.-M. Beuken, R. Caracas, F. Detraux, M. Fuchs, G.-M. Rignanese, L. Sindic, M. Verstraete, G. Zerah, F. Jollet, *et al.*, Comput. Mater. Sci. **25**, 478 (2002).
[118] X. Gonze, Z. Kristallogr. Cryst. Mater. **220**, 558 (2005).
[119] X. Gonze, B. Amadon, P.-M. Anglade, J.-M. Beuken, F. Bottin, P. Boulanger, F. Bruneval, D. Caliste, R. Caracas, M. Côté, *et al.*, Comp. Phys. Commun. **180**, 2582 (2009).
[120] X. Gonze, F. Jollet, F. A. Araujo, D. Adams, B. Amadon, T. Applencourt, C. Audouze, J.-M. Beuken, J. Bieder, A. Bokhanchuk, *et al.*, Comput. Phys. Commun. **205**, 106 (2016).
[121] A. H. Romero, D. C. Allan, B. Amadon, G. Antonius, T. Applencourt, L. Baguet, J. Bieder, F. Bottin, J. Bouchet, E. Bousquet, F. Bruneval, G. Brunin, D. Caliste, M. CÃŽtÃ©, J. Denier, C. Dreyer, P. Ghosez, M. Giantomassi, Y. Gillet, O. Gingras, D. R. Hamann, G. Hautier, F. Jollet, G. Jomard, A. Martin, H. P. C. Miranda, F. Naccarato, G. Petretto, N. A. Pike, V. Planes, S. Prokhorenko, T. Rangel, F. Ricci, G.-M. Rignanese, M. Royo, M. Stengel, M. Torrent, M. J. van Setten, B. Van Troeye, M. J. Verstraete, J. Wiktor, J. W. Zwanziger, and X. Gonze, The Journal of Chemical Physics **152**, 124102 (2020).
[122] D. Hamann, Phys. Rev. B **88**, 085117 (2013).
[123] S. Baroni, S. De Gironcoli, A. Dal Corso, and P. Giannozzi, Rev. Mod. Phys. **73**, 515 (2001).
[124] X. Gonze, Phys. Rev. A **52**, 1096 (1995).
[125] E. McCann, Phys. Rev. B **74**, 161403 (2006).
[126] M. Sui, G. Chen, L. Ma, W.-Y. Shan, D. Tian, K. Watanabe, T. Taniguchi, X. Jin, W. Yao, D. Xiao, *et al.*, Nat. Phys. **11**, 1027 (2015).

Supplemental Materials

Thicker Slabs of $Mg_nB_{2n}C_2$

Note: *More information will be added to the SM.*

The most general form of this 2D material is obtained by replicating the inner layers of MgB_2 shown by the dashed rectangular area in Fig. 1(b). Thus resulting slab is similar to a MgB_2 slab but with inert surfaces of B-C layers, instead of B-B surfaces in a MgB_2 slab. The calculated band structures of $Mg_nB_{2n}C_2$ for $n = 3, 4, 5$ are shown in Fig. 4. As the number of the inner MgB_2 layers increases, the σ subbands create a more MgB_2-like bandstructure (almost independent of k_z in bulk). This is a strong indication of transference of the superconducting properties from the bulk to quasi-2D.

The behavior of the p_z bands is more complicated, with extra degenerate band crossings near the Dirac points at K and K′ high symmetry points. These degeneracies are expected as long the inversion and time-reversal symmetry are preserved. The different on-site energy of the C atom is responsible for avoided crossings near the K and K′ high symmetry points.

Alternative arrangement without inversion symmetry

This 2D material can have two versions depending upon on the ordering of the boron and carbon atoms in the top and bottom surface layers. $Mg_2B_4C_2$ monolayer

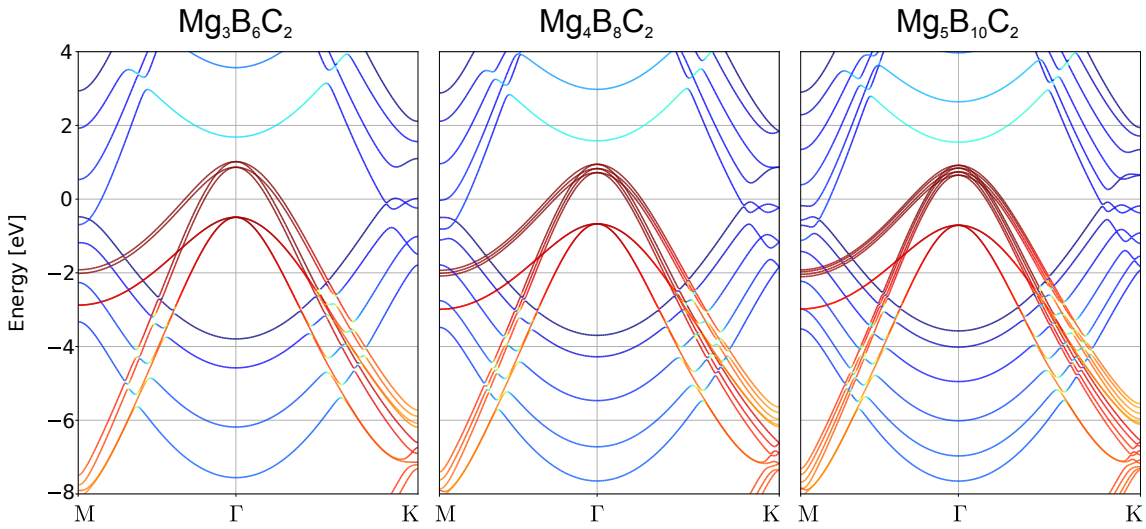

FIG. 4. Band structures of thicker slabs of $Mg_nB_{2n}C_2$. The $p_{x,y}$ σ orbitals are colored red and the p_z orbitals are blueish.

preserves the inversion symmetry if the top and bottom layers are made of B-C and C-B (notice the ordering of atoms). Whereas, the inversion symmetry is broken if the top and bottom layers are made of B-C and B-C (or both C-B). The inversion symmetric structure, discussed in the main text, is $\sim 5\,$meV/f.u. energetically more favorable than the structure with broken inversion symmetry.

Also, if we add a MgB_2 layer to the inversion symmetric $Mg_2B_4C_2$, the resulting system–$Mg_3B_6C_2$– will break the inversion symmetry. In order to preserve this symmetry, we need to interchange the boron and carbon atoms in one B-C layer. The same principle applies for thicker slabs: if the C atoms belong to the same sublattice, the whole system is inversion symmetric (asymmetric) for an odd (even) number of Mg layers.

The lack of inversion symmetry opens a bandgap at the Dirac points, see Fig. 5, in the same way as an external electric field opens a band gap in bilayer graphene [125]. As the low energy representation (p_z bands) of both systems become equivalent, the analogy with bilayer graphene also implies the emergence of the valley Hall effect if a suitable electric field is applied [126]. The magnitude of the band gap, due to inversion asymmetry, is about 0.8 eV for $Mg_2B_4C_2$ monolayer, and it decreases steadily with increasing slab thickness.

Tight-Binding Model

The projection of atomic orbitals on the electronic band structure of $Mg_2B_4C_2$ monolayer is shown in Fig 6(a). The accuracy of our Wannier tight-binding parametrization is shown in Fig. 6(b).

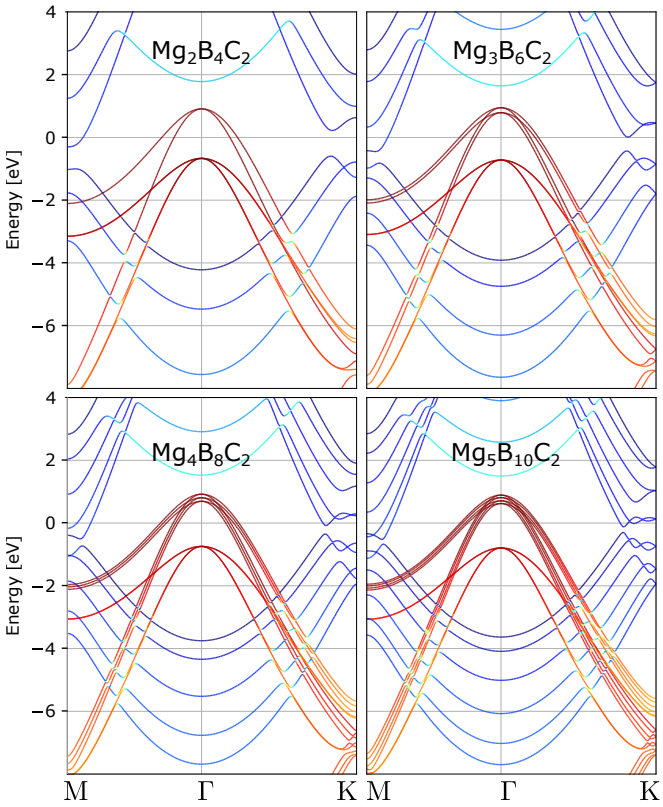

FIG. 5. Electronic band structures of the thicker slabs of $Mg_nB_{2n}C_2$. The $p_{x,y}$ σ orbitals are colored red and the p_z orbitals are blueish.

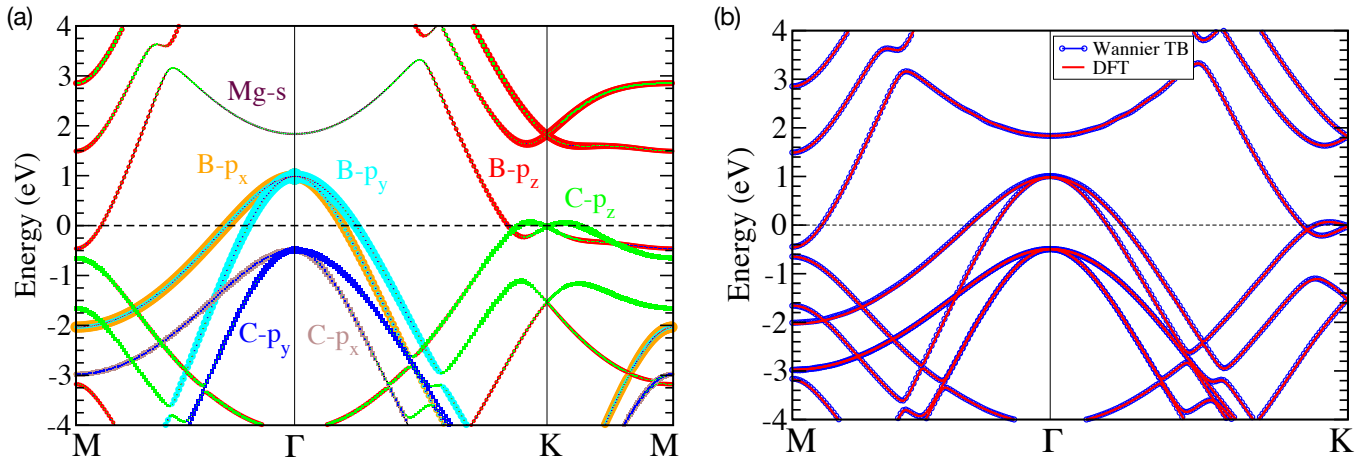

FIG. 6. (a) Atomic orbitals resolved electronic bandstructure calculated without inclusion of SOC (DFT-PBE) for $Mg_2B_4C_2$ monolayer. (b) Comparison of the DFT bandstructure with the same obtained from Wannier tight-binding (TB) model.